1 <u>Potential and Limitations of Finite Element Modelling in Assessing Structural Integrity of</u>

2 <u>Coralline Algae under Future Global Change</u>

3 Running head: Modelling the coralline algal skeleton

4 L.A. Melbourne[123], J. Griffin[1], D.N. Schmidt[1] and E.J. Rayfield[2]

5 1) School of Earth Sciences, University of Bristol, Wills Memorial Building, Queen's

6 Road, BS8 1RJ, Bristol, UK

7 2) School of Earth Sciences, University of Bristol, Life Sciences Building, 24 Tyndall

8 Avenue, BS8 1TQ, Bristol, UK

9 3) Department of Life Sciences, Natural History Museum, Cromwell Road, SW7 5BD,

10 London, UK

11

12 Corresponding Author: Leanne Melbourne, tel +44 (0) 117 954 5243, fax +44 (0)117 954

13 5420, email: l.melbourne@bristol.ac.uk

14   ABSTRACT

15   Coralline algae are important habitat formers found on all rocky shores. While the impact of

16   future ocean acidification on the physiological performance of the species has been well

17   studied, little research has focussed on potential changes in structural integrity in response to

18   climate change. A previous study using 2D Finite Element Analysis (FEA), suggested

19   increased vulnerability to fracture (by wave action or boring) in algae grown under high CO_2

20   conditions. To assess how realistically 2D simplified models represent structural

21   performance, a series of increasingly biologically accurate 3D FE-models that represent

22   different aspects of coralline algal growth were developed. Simplified geometric 3D models

23   of the genus *Lithothamnion* were compared to models created from computed tomography

24   (CT) scan data of the same genus. The biologically accurate model and the simplified

25   geometric model representing individual cells had similar average stresses and stress

26   distributions, emphasizing the importance of the cell walls in dissipating the stress throughout

27   the structure. In contrast models without the accurate representation of the cell geometry

28   resulted in larger stress and strain results. Our more complex 3D model reiterated the

29   potential of climate change to diminish the structural integrity of the organism. This suggests

30   that under future environmental conditions the weakening of the coralline algal skeleton

31   along with increased external pressures (wave and bioerosion) may negatively influence the

32   ability for coralline algae to maintain a habitat able to sustain high levels of biodiversity.

1 INTRODUCTION

Since the pre-industrial era CO_2 concentrations have risen by more than 100ppm (Ciais et al., 2013). The ocean has absorbed approximately 30% of the total anthropogenic CO_2 emissions (Rhein et al., 2013). This has led to a change in the carbonate chemistry of the ocean, resulting in a lowering of the carbonate saturation state and a decrease in ocean pH, a process termed 'ocean acidification' (Caldeira and Wickett, 2003). Future projections suggest an additional average decrease in pH of between 0.13 (RCP 2.6) and 0.42 units (RCP 8.5) by the year 2100 (Pörtner et al., 2014). Calcifying organisms are at risk as the lower carbonate saturation state may affect the ability to calcify shells and skeletons (Diaz-Pulido et al., 2011; Fabricius et al., 2011; Kroeker et al., 2010). In response, ecosystem shifts are predicted to occur; for example sea-grasses and kelps may outcompete calcifying algae as the major habitat formers in shallow water habitats (Fabricius et al., 2011).

Rhodoliths (Fig. 1), non-geniculate free living (live and dead) coralline red algae (Foster, 2001), are an extremely diverse group of benthic calcifying organisms found from the polar to the tropical regions and low intertidal zones to 150m deep (Foster, 2001). They are major contributors to the global inorganic carbon budget in shallow water ecosystems (Mackenzie et al., 2004). The largest rhodolith bed found on the Abrolhos shelf contributes roughly 5% to the global calcium carbonate budget (Amado-Filho et al., 2012). Additionally these benthic ecosystems support a high level of biodiversity by forming structurally and functionally complex habitats (Nelson, 2009) for many organisms including polychaetes, crustaceans and molluscs (Foster, 2001), as well as being important nursery grounds to commercial species including scallops (Grall and Hall-Spencer, 2003). Coralline algae biodiversity and habitat complexity are directly correlated; species richness and abundance of, in particular, arthropods, annelids and cnidarians, are known to increase as rhodolith size and branching increases (Foster et al., 2013). However coralline algae are ecologically fragile due to their

58 slow growth rate of ~1mm yr^{-1} (Freiwald and Henrich, 1994) and sensitivity to physical

59 disturbances such as extraction and dredging.

60 Furthermore, as they form high Mg- calcite skeletons, the most soluble polymorph of calcium

61 carbonate ($CaCO_3$) (Andersson et al., 2008), coralline algae are more susceptible to ocean

62 acidification than other organisms that utilise different polymorphs of calcium carbonate.

63 Consequently, a significant loss of rhodoliths from the North Atlantic by the year 2100 has

64 been predicted (Brodie et al., 2014). However, laboratory experiments have shown highly

65 varied responses to elevated levels of CO_2. Coralline algae (*Neogoniolithon* sp.) and

66 calcareous green algae (*Halimeda incrassata*) exposed to increased CO_2 concentrations (606

67 and 903 ppm for 60 days) showed an increase in calcification (Ries et al., 2009); whereas

68 another study on *Lithothamnion glaciale*, a cold temperate coralline algae, displayed a

69 decrease in growth rate at elevated CO_2 conditions (589 and 755 µatm for three months)

70 (Ragazzola et al., 2012), while also showing evidence for potential acclimation after ten

71 months (Ragazzola et al., 2013).

72 Coralline algae have many pressures to withstand in their natural environments, including

73 wave action and bioerosion, while maintaining a structurally and functionally complex

74 habitat. Under elevated CO_2 conditions the algal skeleton appeared to be weakened

75 (Ragazzola et al., 2012), thereby favouring erosion and breakage (Kamenos et al., 2013;

76 Ragazzola et al., 2012).

77 Finite Element Analysis (FEA) is a technique that reconstructs the stress, strain and

78 deformation in structures (Zienkiewicz et al., 2005). Originally developed for mathematical

79 and engineering applications, it has recently become an established technique in zoology and

80 palaeontology to understand morphology, function and evolution of hard tissue structures

81 (Rayfield, 2007).

82 FEA works by transforming a continuous structure into a discrete number of elements which

83 are connected to each other via nodes. The combination of elements and the interconnecting

84 nodes form the mesh. Appropriate material properties (Young's modulus and Poisson's ratio)

85 are assigned to the elements to mimic the elasticity of the structure. Adequate boundary

86 conditions (magnitude and direction of loading and constraints) are applied and then nodal

87 displacements are calculated in response to the applied boundary conditions and material

88 properties of the model. The nodal displacement is used to calculate the strain and

89 subsequently stress (using the Young's modulus, see equation 1) and hence mechanical

90 performance of complex structures can be inferred. (For mathematical equations see

91 Mathematics of FEA, (Rayfield, 2007) supplementary material)

92 E (Young's modulus) = σ (stress)/ ε (Strain)   (1)

93 Ragazzola et al. (2012) were the first to use FEA in ocean acidification studies by creating

94 simple 2D FE-models of coralline algae to quantify the effect of elevated CO_2 on the skeleton

95 of *Lithothamnion glaciale*. Although the changes in growth rate were not significant,

96 specimens grown under CO_2 conditions predicted for the year 2050 were found to have

97 significantly larger cells and thinner cell walls. These ultrastructure changes resulted in

98 predicted increased vulnerability to fracture compared to present day structures (Fig. 2a-b) as

99 observed in the 2D FE-model.

100 These simple 2D models represented the mechanical performance of a cross-section of

101 uniform thickness (1µm) (Ragazzola et al., 2012) through the algal structure. However, these

102 highly innovative models were simplistic in nature. Importantly, they had not been tested to

103 assess if they were a fair representation of skeletal mechanical performance. Consequently,

104 the simple 2D model may have overestimated the distribution and magnitude of stress and

105 hence future vulnerability of algal communities. Here we have developed a set of 3D FE

106   geometric models to represent different aspects of coralline algae morphology and compared

107   these models with a more biologically accurate 3D FE-model generated from computed

108   tomography (CT) data, allowing us to assess the trade-off between computing time (Andersen

109   and Jones, 2006; Romeed et al., 2006) and the need for an appropriate representation of the

110   structure.

111   We then used our improved understanding of the performance of the 3D models to re-assess

112   the impact of current and future ppm CO_2 induced changes to morphology on the ability of

113   algal communities in maintaining a high level of biodiversity. Finally, the loading and

114   constraint taken from Ragazzola et al. (2012) were a mixture of shear and compressive

115   forces, which simulated boring forces by an organism exerted on the exposed corner of an

116   attached thallus. As it was assumed that these organisms were more prone to shear forces

117   than compressive ones, we also assessed the effect of sole compressive or sole shear forces

118   on the compartmentalised and the biologically realistic model.

2   MATERIALS AND METHODS

2.1   Model Geometry

Four 3D FE-models with different coralline algal features were created based on the

measurements and properties of Ragazzola et al. (2012) models. All 3D geometric models

were created and analysed in the Finite Element software package, Abaqus/CAE, v.6.10,

(Simula, USA, Dassault Systémes, //Simula, Providence, RI, USA), following the protocol

established by Ragazzola et al (2012).

Firstly, the 2D models from Ragazzola et al. (2012) were expanded, using the extrude

command in Abaqus, to create a 3D model with the same area, all length and width

dimensions (78.92 x 72.46 μm) were unchanged, but a depth of 80 μm was used instead of 1

μm. Size of the individual cells mirrored that of the 422 μatm model of Ragazzola et al.

(2012), with an individual cell height of 6.3 μm and width of 5.15 μm and an inter- and intra-

wall thicknesses of 2.68 μm and 0.86 μm respectively. This structure is assigned the label

'Corridor model' (Fig. 3a).The inter-wall thickness was the thickness of a single cell wall in

the x direction (between filaments). Therefore the internal walls of the model had two inter

cell walls, whereas the external walls (the left outermost and right outermost) only had one

inter cell wall each. The intra-cell thickness was the cell wall thickness between cells in the

y-direction. As the rhodolith grows as a set of filaments, there was only one cell wall between

two cells in the y-direction (Fig.4).

2.1.1   Compartmentalised (Individual Cell) model with current/ 422 μatm CO_2 cell size

Although the cellular width and height in the Corridor model represented the dimensions

recorded by Ragazzola et al. (2012) from SEM images, the cells are not represented as

discrete entities and instead are represented as hollow calcite 'tubes'. As algal cells grow

apically, they form a lattice of individual cells, hence a second model, 'Compartment model'

(Fig. 3b) was created in which cell walls were added in the Z direction to create discrete

144 cellular spaces. All dimensions apart from the depth of the individual cells and divisions

145 between cells in the z direction were the same as the corridor model. It was assumed the

146 depth of the cell was the same as the width (5.15 µm) and the divisions between the cells in

147 the z direction were the same as the inter cell wall divisions (2.68 µm).

148 **2.1.2 Biologically realistic model**

149 Computed tomography (CT) scans of L. *glaciale* derived from the TOMCAT beamline at the

150 Swiss Light source, Switzerland (see Ragazzola et al, 2012) were imported into *Avizo* V8.0

151 (VSG) software package. Each scan was 150 projections over 180° using a 15 keV energy

152 beam with UPLAPO 10x objective. The field of view was 1.5 x 1.5mm^2 and the pixel size

153 was 0.74 x 0.74 mm^2. A 3D cube of similar dimensions (80 x 80 x 80 µm) as the geometric

154 models was created but instead capturing the actual morphology of the rhodolith (known as

155 the 'Biological model') (Fig. 3c). The cube was selected at random within the scan of the

156 rhodolith (Fig. 5 a-d), as the summer winter layers could not be distinguished in the CT scan.

157 The scans were thresholded in *Avizo* and then exported to *Hypermesh* (v.11; part of the

158 *Hyperworks* package from Altair, MI, USA) to create FE-models, which were analysed in

159 *Abaqus* v6.10.

160 **2.1.3 Compartmentalised (Individual Cell) model with 2050 / 589 µatm CO_2 cellular**
161 **size**

162 A final model, 'the OA model' (Fig. 3d), was created by adjusting the cell size and spacing to

163 represent the dimensions of the future 589 µatm CO_2 model as a 3D and compartmentalised

164 structure with overall dimensions (74.99 x 77.2 x 80 µm), individual cell dimensions (11.7 x

165 7.99 x7.99 µm) and intra and inter-cell wall dimensions (0.685 µm and 0.829 µm

166 respectively). This future predicted CO_2 model was compared to the performance of the 3D

167 compartment model with current CO_2 ppm cell size.

2.2 Finite element analysis (FEA)

2.2.1 Boundary conditions

In keeping with Ragazzola et al. (2012), a load pressure of 20,000 Pa was applied to the top

left corner, 40 μm along the external top surface and 40 μm down the left surface of the

models. Constraints were applied to the whole bottom surface and on the right hand surface,

opposite the loads, 40 μm up from the constrained bottom (Fig. 6). This simulated the

attachment of the structure to the rest of the thallus. Even though the same loads as Ragazzola

et al. (2012) were used, it is known that the primary hydrodynamic force exerted on marine

macroalgae is drag force (Carrington, 1990). Drag (F_{drag}) force can be calculated using

equation 2.

$$Fdrag = \frac{1}{2}(\rho U^2 AC_d) \tag{2}$$

Where ρ is the seawater density (approximately 1025 kg m^{-3}); and U is water velocity.

Subtidal marine macroalgae experience a water velocity on the order of magnitude of 1 m s^{-1}

(Carrington, 1990), while intertidal species can experience breaking waves of up to 25 m s^{-1}

(Denny et al., 2003). A is the algal planform area; and C_d the drag coefficient (dimensionless

index of shape change and reconfiguration of flexible fronds (Carrington, 1990; Dudgeon and

Johnson, 1992; Gaylord et al., 1994)). However, there are no data published for resulting in

breakage of rhodoliths, instead the existing literature focused on flexible macroalgae, making

it difficult to find loads that are environmentally significant whilst also being species related.

2.2.2 Element type and size

Convergence tests were performed for each mesh type in order to determine the minimum

mesh size required. The mesh size was decreased until the average von Mises value no longer

changed relative to mesh size. Hypothetically, all refined meshes should converge to similar

results yet our converged von Mises stress value was an order of magnitude different between

the hexagonal and tetrahedral mesh. This was due to the shape of the tetrahedral elements and

193 the way tetrahedral elements interlock together, making a tetrahedral model stiffer than a

194 hexagonal model. Whereas Dumont et al. (2005) found that comparing a converged 4-node

195 linear and a stiffer 10-node quadrilateral tetrahedral mesh of the same model gave different

196 mean stress values, but within 10%. This shows that even when comparing different forms of

197 the same tetrahedral element, variation in stress is still apparent. Hence when comparing

198 different element types (hexagonal and tetrahedral), we find an even greater difference in

199 variation. Therefore in order to compare the 2D to 3D geometric models, the corridor model

200 was meshed with 4- node linear hexagonal elements. As tetrahedral elements were better at

201 capturing the complex geometry of the biological model and to account for variation in

202 results depending on element type, all models were then meshed with 4-node linear

203 tetrahedral elements in order to be compared to the biologically realistic model and to each

204 other.

205 **2.2.3   Material Properties**
206 In keeping with Ragazzola et al. (2012), all models were assumed to be composed of a

207 linearly elastic, isotropic, homogeneous material with a Young's Modulus of 36 GPa and a

208 Poisson ratio of 0.31 (properties of calcite) (Tanur et al., 2010). Even though these material

209 properties do not accurately represent the heterogeneities in the specimen and their material

210 properties this approach gives a comparative insight into how different geometries affect the

211 overall strength of a structure.

212 Initially, to analyse how sensitive the models were to changing material properties, a set of

213 2D and 3D corridor models with different Young's modulus (maximum and minimum

214 Young's modulus values of two different bivalves – *Mytilus edulis* and *M. californianus*)

215 were analysed.

2.2.4 Displaying and recording results

In order to compare the impact of predators on the different 3D geometric models, stress and

strain results were calculated. Stress, generated by the applied load (force) on a given area, is

represented by the von Mises stress, a function of each of the principle stresses that represents

tensile or compressive stress (Rayfield, 2007). Average stresses were calculated by dividing

the von Mises stress by the element size to account for differing number of elements between

models. Total strain energy refers to the energy stored in a system as a load is applied, which

is a useful variable to record in mineralized structures as the more strain in a system leads to a

larger amount of potential energy available for fracture (Gordon, 1978). The 95th percentile of

(Mises) stress was additionally used as a comparison between the corridor, compartment and

biological models as this metric highlighted the extremes of the von Mises Stress distribution

– an important parameter to highlight fracture potential.

Stress and strain energy are linearly dependent on surface area and volume respectively

(Dumont et al., 2009), hence the applied pressure was rescaled for the biological model to

rule out the effect of increased Mg-calcite volume on modelling stress and strain. To account

for the increase in volume of calcite between the 2D and the 3D model, as strain energy is

dependent on volume, the strain energy was calculated for the 3D model using equation 3,

outlined by Dumont et al. (2009);

$$U_{B*} = (V_B/V_A)^{1/3} (F_A/F_B)^2 U_B \tag{3}$$

where U_{B*} is the total strain energy for model B corrected for calcite volume, V_A and V_B are

the volumes for the models A and B respectively, F_A and F_B are the loads applied to the two

models and U_B is the total strain energy for model B.

The von Mises stress was displayed graphically on the model, with warm colours

(red/orange) indicating areas of high stress and cool colours (blue) indicating areas of low

stress. Stress distribution throughout the model was very similar to surface stress distribution.

The surfaces of the model were more sensitive to the loads and constraints, due to immediate

contact with the boundary conditions. The minimum and maximum von Mises stress values

were found on the surfaces of the models, being more influenced by the position of the

boundary conditions and complexities in the geometry. Hence, the minimum and maximum

values did not provide any additional information on the overall structural integrity of the

model than that provided by the surface contour plots. Average stress values, total strain

energies and 95th percentile of (Mises) stress can be found in Table 1.

2.3   Comparison between shear and compressive loading

The biological and the compartment model were exposed to different loading scenarios in

Abaqus. This included the original load setup explained earlier in section 2.1.4 (Fig. 7a); the

compressive loads, where the load was applied to the top of the cube opposite the constraint

(Fig. 7b); and shear loads, where the load was applied on the face adjacent to the bottom

constraint (Fig. 7c).

As this part of the study moved on from the initial research of Ragazzola et al. (2012), it was

decided to use loads defined experimentally based on real wave velocities. Starko et al.

(2015) used wave velocities of up to 3.5 m s^{-1} to assess the effect of branching in flexible

wave swept macroalgae, in which they also measured the drag force. Water velocity

experienced by subtidal marine macroalgae is on the order of magnitude of 1 m s^{-1}

(Carrington, 1990). Hence, we used a drag force (0.9N) measured for a heavily branched

macroalgae (similar in branching to our rhodoliths) with an algal planform area of 48.20 cm^2

that experienced a wave velocity of 3.5 m s^{-1} to carry out our load type comparison tests

(Starko et al., 2015). Here we have kept the force per unit area constant in order to compare

the compartment model to the biological model. Strain energy is dependent on volume,

therefore in order to compare the total strain energy between the models we had to take into

265   account the difference in calcite volume between the biological model and the compartment

266   model (using equation 3) (Dumont et al., 2009).

3   RESULTS

A similar stress distribution was observed in the 2D and 3D geometric model (Corridor model) (Fig. 8a-b), with areas of high stress occurring along the intra-cell walls and adjacent to the constrained surface. The average von Mises stress of the two models was very similar (Table 1), indicating that the simple 2D model (Fig. 8a) was an accurate representation of the stress in a simple 3D geometric model (Fig. 8b). As expected, the total strain energy in the 3D model was over 500x higher than the 2D model, showing that the 3D model with a larger volume was able to store more than the relative amount of strain energy compared to the 2D model.

Once the complexity of the 3D model was increased to better represent the natural structural complexity, differences between the simple 3D model (Corridor model) and the more complex models became evident (Fig. 9a-c). In the compartment model of current CO_2 conditions (Fig. 9b), both, the average stress and total strain energies were lower than the Corridor model (63% and 76% respectively) (Table 1). The addition of cellular walls in the Z direction removed regions of peak stress near the constraints as stresses now dissipated throughout the structure, stabilising the model.

The results of the comparison between the 3D geometric models (the Corridor and Compartment model) and the realistic model of similar dimensions generated from CT scans (the Biological model) showed that a similar average stress, strain energy (Table 1) and stress distribution (Fig. 9b-c) was observed between the compartment model and the biological model. Comparison of the internal morphology between the compartment model and the biological model also showed similarities. Both models had regularly distributed cavities. However unlike the compartment model the biological model cavities were spheroidal and, due to the natural variation within these specimens, the arrangement of cavities was not as regimented as in the compartment model (Fig. 10). Both the biological model and the

292   compartment model had the same percentage volumes of calcite and cavities whereas the

293   corridor model had a lower percentage volume of calcite (Table 2).

294   As the compartment model was similar in performance to the biological model, we used this

295   model to assess the impact of ocean acidification (Fig. 2c-d). The change in wall thickness

296   and cell size in the 589 µatm/ 2050 model led to a near doubling of average stress and a

297   doubling of the total strain energy (Table 1). This increase in strain energy was less than

298   suggested using the simple 2D models, which predicted an increase in average stress of 309%

299   and strain energy of 1421%.

300   However, using more environmentally significant forces in the shear and compressive

301   comparison tests, we can see that the stresses and strains exerted by these organisms were not

302   as large as those taken from Ragazzola et al. (2012). Accounting for the change in units, the

303   differences between the von Mises stress results (Pa) are on the order of magnitude of 10^9

304   instead of 10^{11}.

305   In the biological model, under the original load setup, stress dissipated throughout the model

306   from the corner where the load was applied to the constrained corner (Fig. 7a). While under

307   the compressive load setup, the stress had a top to bottom distribution (from the loaded

308   surface to the constrained surface) with a slight increase in stress surrounding the cavities in

309   the model (Fig. 7b) and under the shear load setup, two thin bands of higher stress

310   perpendicular to each other were observed (Fig. 7c). The average von Mises Stress, 95th

311   percentile of (Mises) stress and total strain energy were slightly larger under the shear load

312   setup compared to the compressive load setup (Table 3). All three values were larger than the

313   compressive or shear model in the original load set up (Table 3).

314   In the compartment model, under the original load setup the stress dissipated throughout the

315   model from the corner where the load was applied to the constrained corner (Fig. 7d). While

316   under the compressive load setup, the area of higher stress was restricted to the top of the

317   model where the load was applied (Fig. 7e) and under the shear load setup, the area of high

318   stress spread from the right hand side near the constrained corner (Fig. 7f). The average von

319   Mises stress, 95th percentile of (Mises) stress and the total strain energy were largest under

320   sole shear loads and smallest in the compressive load model, with values for the original set

321   up falling in between (Table 3).

322   Note the shear load in the compartment model was applied differently to the arrangement for

323   the biological model. As the compartment model was not able to run under a sole shear load,

324   like the biological model, a small constraint on the opposite face (1µm) was added to help

325   stabilise the model (Fig. 7f). The compartment model did not run under the sole shear load as

326   it experienced extremely high stresses at the interface between the bottom constraint and the

327   adjacent unconstrained surface.

328   The sensitivity test of the 2D model and the 3D corridor model highlighted that increasing the

329   Young's modulus by 120% did not result in any change in stress, whereas the total strain

330   energy decreased with increasing Young's modulus (Table 4).

4   DISCUSSION

Ragazzola et al. (2012) used 2D FE-models to predict if changes to coralline algae cellular morphology induced by higher CO_2 concentrations generate a structure that might less able withstand stresses compared to current specimens. They predicted that increased CO_2 and resulting ocean acidification will create a structure more susceptible to fracture in response to environmental stressors such as wave action and boring. This 2D model was the first step in assessing the structural and mechanical consequences of high CO_2-induced changes to growth structure, but it is important to note that it represented a 2D approximation of a complex 3D structure. Here our results showed that a 3D extrapolation of the 2D FE-model (Corridor model) generated comparable patterns and magnitudes of average stress to the 2D model. However, once the complexity of the 3D model was altered to approximate cellular compartments and compared to a biologically realistic model generated from SRXTM data, it became clear that stress and strain energy magnitudes in the simple 2D and 3D models were an over-estimation.

Coralline algae grow apically with lateral cell fusion being very common (Irvine and Chamberlain, 1994). This creates a vast network of individual cells able to oppose stress in all directions (Gordon, 1978). The importance of these structures is highlighted by the geometric model with compartments (the Compartment model) being the most stable of the geometric structures assessed and also most comparable – in terms of percentage volume of calcite, stress distribution and magnitudes of average stress and total strain energy – to the biological model (Table 1 & 2). This highlights the importance of geometry changes, which our method accurately captured, to the distribution and magnitude of stress. This occurrence was also observed by Romeed et al. (2006) who previously found that changes in the geometry between their 2D and 3D models of a restored premolar tooth also affected their displacement and profile stresses.

356   Creating the FE-model of the biologically realistic structure (the Biological model) from

357   SRXTM data was a time consuming process compared to the user effort required to generate

358   the compartmentalised geometric model (the Compartment model). As these different models

359   produced very similar measures of average stress (2.75E+10 Pa compared to 2.74E+10 Pa for

360   the geometric and the biological model respectively), comparable measures of total strain

361   energy (4.28E09 J compared to 5.21E09 J) and a similar stress distribution, we propose that

362   the compartment model presented a time efficient opportunity to manipulate geometric

363   features to test hypotheses of mechanical performance and structural integrity.

364   Hence this model was used to assess the impact of ocean acidification changes to the cell

365   growth on structural integrity. When the cellular size of the 3D model was adjusted to reflect

366   589 µatm growth conditions, the structure was less 'efficient' than the structure under current

367   environmental conditions, with a higher average stress and total strain energy. It is important

368   to note that the increase in stress and total strain energy magnitude was less pronounced than

369   that suggested by the 2D models, indicating that the extra cellular walls aided in stabilising

370   the thinner cell walls of the model. This finding was in agreement with other work showing

371   that microstructural features affect the mechanical properties of cellular solids (Gibson,

372   2005). For example, wood has a stiffness to weight ratio equal to steel, which is partly due to

373   the arrangement of cells in a honeycomb structure (Gibson et al., 2010). Hence these features

374   provide habitat forming organisms with a larger structural integrity to withstand external

375   pressures and the ability to live in a highly dynamic environment such as the coastal shelf.

376   Although our geometric and biological models show congruence, they are still simplifications

377   of the heterogeneities in the algal skeleton. A factor which was not considered in this study is

378   the potential effect of changing material properties due to global change on the algal skeleton.

379   Material properties are affected by the concentration of Mg in the skeleton (Ma et al., 2008),

380   which is dependent on temperature (Kamenos et al., 2008) and potentially pH (Ragazzola et

381 al., 2013; Ries, 2011). Mg incorporated into the calcite lattice increases the lattice distortion,

382 which causes an increase in the sliding resistance and deformation resistance to crystals

383 (Wang et al., 1997). Ma et al. (2008) found that due to a much larger difference in mol% of

384 $MgCO_3$ (just below 40%), the high Mg-calcite polycrystalline matrix of the tooth of a sea

385 urchin had a significantly higher elastic modulus (E) and hardness (H) value than both

386 synthetic calcite and the single crystalline needles.

387 Sea surface temperatures in the North Atlantic are predicted to rise 2.5°C by the end of the

388 century (Rhein et al., 2013). This rise in temperature corresponds to a 3% increase in mol%

389 of $MgCO_3$ (Kamenos et al., 2008). As a 3% change in mol% of $MgCO_3$ is within the natural

390 variation between specimens (Ragazzola et al., 2013), we suggest such a mol% change in

391 $MgCO_3$ will not significantly impact the material properties and hence affect the skeleton .

392 However Ma et al. (2008) also suggested the large difference in material properties wasn't

393 due to just the difference in mol% of $MgCO_3$ but also due to the orientation and uniform size

394 of the crystals. This illustrates that Mg/Ca ratios are not the only factor which affects

395 material properties.

396 Proteins are also known to affect material properties as the incorporation of organic

397 macromolecules reduces the brittleness and enables plastic deformation (Berman et al., 1988;

398 Ma et al., 2008; Wang et al., 1997; Weiner et al., 2000). The presence of chitin and collagen

399 within the skeleton of *Clathromorphum compactum* aids calcification and increase skeletal

400 strength (Rahman and Halfar, 2014). Implementing accurate material properties specific for

401 specimens grown under a wide range of conditions into the model would allow a more

402 accurate assessment of whether phenotypic variability in material properties has the potential

403 to counteract structural changes in response to ocean acidification.

404   However, using these more biologically accurate models, we have further supported previous

405   results that state future climate change will lead to a loss in the structural integrity of coralline

406   algae. We have shown that by increasing the complexity of a simple 2D geometric model to a

407   3D geometric model we can obtain informative data on the effect of ocean acidification on

408   the structural integrity of the coralline algal skeleton, without need for complex real

409   biological models derived from CT scanning that take ample computer time to construct and

410   analyse. As responses to climate change are species-specific, we are therefore able to create

411   models tailor made to individual species and analyse how they react to future climate change.

412   We have also shown the susceptibility these models have to shear loads rather than

413   compressive loads.

414   As the oceans are becoming more acidic, with concurrent calcification pressure, it is vital to

415   understand the potential effect of ocean acidification on the skeletons of these habitat forming

416   organisms to infer whether they are able to maintain habitats in the future. As coralline algae

417   are major habitat formers, with the diversity and abundance of species dependent on their

418   structural complexity, weakening of the skeleton under high CO_2 conditions will affect the

419   organisms that rely on coralline algae as a habitat with important consequences for marine

420   ecosystems. Our model results, along with bioerosion, rising sea levels (Rhein et al., 2013)

421   and predicted increases in frequency and intensity of storm surges (Knutson et al., 2010)

422   strongly suggest that coralline algae will be under more intense environmental pressure in

423   future CO_2 scenarios.

424   It is important to note that recent long term studies have shown calcifying organisms

425   acclimating to ocean acidification for example cold water corals sustaining growth rates

426   (Form and Riebesell, 2012) or coralline algae decreasing growth rates to maintain cell wall

427   thickness (Ragazzola et al., 2013). The consequence of this sustained growth on the material

428   properties and structural integrity has not been assessed and poses an open question with

429   regards to their ability to provide habitats in the future.

AUTHOR CONTRIBUTIONS

430

431 Leanne Melbourne and Julia Griffin carried out the experiments under the guidance of

432 Daniela Schmidt and Emily Rayfield. Leanne Melbourne prepared the manuscript with

433 contributions from all co-authors.

REFERENCES

Amado-Filho, G. M., Moura, R. L., Bastos, A. C., Salgado, L. T., Sumida, P. Y., Guth, A. Z., Francini-Filho, R. B., Pereira-Filho, G. H., Abrantes, D. P., Brasileiro, P. S., Bahia, R. G., Leal, R. N., Kaufman, L., Kleypas, J. A., Farina, M., and Thompson, F. L.: Rhodolith Beds Are Major $CaCO_3$ Bio-Factories in the Tropical South West Atlantic, PLoS ONE, 7, e35171, 2012.

Andersen, L. and Jones, C.: Coupled boundary and finite element analysis of vibration from railway tunnels—a comparison of two-and three-dimensional models, Journal of Sound and Vibration, 293, 611-625, 2006.

Andersson, A. J., Mackenzie, F. T., and Bates, N. R.: Life on the margin: implications of ocean acidification on Mg-calcite, high latitude and cold-water marine calcifiers, Mar Ecol Prog Ser, 373, 265-273, 2008.

Berman, A., Addadi, L., and Weiner, S.: Interactions of sea-urchin skeleton macromolecules with growing calcite crystals - a study of intracrystalline proteins, Nature, 331, 546-548, 1988.

Brodie, J., Williamson, C. J., Smale, D. A., Kamenos, N. A., Mieszkowska, N., Santos, R., Cunliffe, M., Steinke, M., Yesson, C., Anderson, K. M., Asnaghi, V., Brownlee, C., Burdett, H. L., Burrows, M. T., Collins, S., Donohue, P. J. C., Harvey, B., Foggo, A., Noisette, F., Nunes, J., Ragazzola, F., Raven, J. A., Schmidt, D. N., Suggett, D., Teichberg, M., and Hall-Spencer, J. M.: The future of the northeast Atlantic benthic flora in a high CO_2 world, Ecology and Evolution, 4, 2787-2798, 2014.

Caldeira, K. and Wickett, M. E.: Oceanography: anthropogenic carbon and ocean pH, Nature, 425, 365-365, 2003.

Carrington, E.: Drag and dislodgment of an intertidal macroalga: consequences of morphological variation in Mastocarpus papillatus Kützing, Journal of Experimental Marine Biology and Ecology, 139, 185-200, 1990.

Ciais, P., Sabine, C., Bala, G., Bopp, L., Brovkin, V., Canadell, J., Chhabra, A., DeFries, R., Galloway, J., Heimann, M., Jones, C., Quéré, C. L., Myneni, R. B., and Thornton, S. P. a. P.: Carbon and Other Biogeochemical Cycles. In: Climate Change 2013: The Physical Science Basis. Contribution of Working Group I to the Fifth Assessment Report of the Intergovernmental Panel on Climate Change (eds Stocker, T.F., Qin, D., Plattner, G.K., Tignor, M., Allen, S.K., Boschung, J., Nauels, A., Xia, Y., Bex, V. and Midgley, P.M.),. Cambridge University Press, Cambridge, United Kingdom and New York, NY, USA., 2013.

Denny, M. W., Miller, L. P., Stokes, M. D., Hunt, L. J. H., and Helmuth, B. S. T.: Extreme Water Velocities: Topographical Amplification of Wave-Induced Flow in the Surf Zone of Rocky Shores, Limnology and Oceanography, 48, 1-8, 2003.

Diaz-Pulido, G., Gouezo, M., Tilbrook, B., Dove, S., and Anthony, K. R. N.: High CO2 enhances the competitive strength of seaweeds over corals, Ecology Letters, 14, 156-162, 2011.

Dudgeon, S. R. and Johnson, A. S.: Thick vs. thin: thallus morphology and tissue mechanics influence differential drag and dislodgement of two co-dominant seaweeds, Journal of Experimental Marine Biology and Ecology, 165, 23-43, 1992.

Dumont, E., Grosse, I., and Slater, G.: Requirements for comparing the performance of finite element models of biological structures, Journal of Theoretical Biology, 256, 96-103, 2009.

Dumont, E. R., Piccirillo, J., and Grosse, I. R.: Finite-element analysis of biting behavior and bone stress in the facial skeletons of bats, The Anatomical Record Part A: Discoveries in Molecular, Cellular, and Evolutionary Biology, 283A, 319-330, 2005.

Fabricius, K. E., Langdon, C., Uthicke, S., Humphrey, C., Noonan, S., De'ath, G., Okazaki, R., Muehllehner, N., Glas, M. S., and Lough, J. M.: Losers and winners in coral reefs acclimatized to elevated carbon dioxide concentrations, Nature Climate Change, 1, 165-169, 2011.

Form, A. U. and Riebesell, U.: Acclimation to ocean acidification during long-term CO2 exposure in the cold-water coral Lophelia pertusa, Global Change Biology, 18, 843-853, 2012.

Foster, M. S.: Rhodoliths: between rocks and soft places, Journal of Phycology, 37, 659-667, 2001.

492   Foster, M. S., Amado Filho, G. M., Kamenos, N. A., Riosmena-Rodríguez, R., and Steller, D. L.:
493   Rhodoliths and Rhodolith Beds, Smithsonian Contributions to the Marine Sciences; no. 39, 2013.
494   143-155, 2013.
495   Freiwald, A. and Henrich, R.: Reefal coralline algal build-ups within the Arctic Circle: morphology and
496   sedimentary dynamics under extreme environmental seasonality, Sedimentology, 41, 963-984, 1994.
497   Gaylord, B., Blanchette, C. A., and Denny, M. W.: Mechanical Consequences of Size in Wave-Swept
498   Algae, Ecological Monographs, 64, 287-313, 1994.
499   Gibson, L. J.: Biomechanics of cellular solids, Journal of Biomechanics, 38, 377-399, 2005.
500   Gibson, L. J., Ashby, M. F., and Harley, B. A.: Cellular materials in nature and medicine, Cambridge
501   University Press, New York, 2010.
502   Gordon, J.: Structures: or Why Things Don't Fall Down, Penguin Books, New York, 1978.
503   Grall, J. and Hall-Spencer, J. M.: Problems facing maerl conservation in Brittany, Aquatic
504   Conservation: Marine and Freshwater Ecosystems, 13, S55-S64, 2003.
505   Irvine, L. M. and Chamberlain, Y. M.: Volume 1 Rhodophyta Part 2B Corallinales, Hildenbrandiales,
506   Natural History Museum, London, 1994.
507   Kamenos, N., Cusack, M., and Moore, P.: Coralline algae are global palaeothermometers with bi-
508   weekly resolution, Geochimica et Cosmochimica Acta, 72, 771-779, 2008.
509   Kamenos, N. A., Burdett, H. L., Aloisio, E., Findlay, H. S., Martin, S., Longbone, C., Dunn, J.,
510   Widdicombe, S., and Calosi, P.: Coralline algal structure is more sensitive to rate, rather than the
511   magnitude, of ocean acidification, Global change biology, 19, 3621-3628, 2013.
512   Knutson, T. R., McBride, J. L., Chan, J., Emanuel, K., Holland, G., Landsea, C., Held, I., Kossin, J. P.,
513   Srivastava, A., and Sugi, M.: Tropical cyclones and climate change, Nature Geoscience, 3, 157-163,
514   2010.
515   Kroeker, K. J., Kordas, R. L., Crim, R. N., and Singh, G. G.: Meta-analysis reveals negative yet variable
516   effects of ocean acidification on marine organisms, Ecology letters, 13, 1419-1434, 2010.
517   Ma, Y., Cohen, S. R., Addadi, L., and Weiner, S.: Sea Urchin Tooth Design: An "All-Calcite"
518   Polycrystalline Reinforced Fiber Composite for Grinding Rocks, Advanced Materials, 20, 1555-1559,
519   2008.
520   Mackenzie, F. T., Lerman, A., and Andersson, A. J.: Past and present of sediment and carbon
521   biogeochemical cycling models, Biogeosciences, 1, 11-32, 2004.
522   Nelson, W.: Calcified macroalgae–critical to coastal ecosystems and vulnerable to change: a review,
523   Marine and Freshwater Research, 60, 787-801, 2009.
524   Pörtner, H. O., Karl, D., Boyd, P. W., Cheung, W., Lluch-Cota, S. E., Nojiri, Y., Schmidt, D. N., and
525   Zavialov, P.: Ocean systems. In: Climate Change 2014: Impacts, Adaptation, and Vulnerability. Part A:
526   Global and Sectoral Aspects. Contribution of Working Group II to the Fifth Assessment Report of the
527   Intergovernmental Panel of Climate Change (eds Field, C.B., Barros, V.R., Dokken, D.J., Mach, K.J.,
528   Mastrandrea, M.D., Bilir, T.E., Chatterjee, M., Ebi, K.L., Estrada, Y.O., Genova, R.C., Girma, B., Kissel,
529   E.S., Levy, A.N., MacCracken, S., Mastrandrea, P.R. and

530   White, L.L.), Cambridge University Press, Cambridge, United Kingdom and New York, NY, USA, 411-
531   484 pp., 2014.
532   Ragazzola, F., Foster, L. C., Form, A., Anderson, P. S. L., Hansteen, T. H., and Fietzke, J.: Ocean
533   acidification weakens the structural integrity of coralline algae, Global Change Biology, 18, 2804-
534   2812, 2012.
535   Ragazzola, F., Foster, L. C., Form, A. U., Buscher, J., Hansteen, T. H., and Fietzke, J.: Phenotypic
536   plasticity of coralline algae in a High CO_2 world, Ecology and Evolution, 3, 3436-3446, 2013.
537   Rahman, M. A. and Halfar, J.: First evidence of chitin in calcified coralline algae: new insights into the
538   calcification process of Clathromorphum compactum, Sci. Rep., 4, 2014.
539   Rayfield, E. J.: Finite element analysis and understanding the biomechanics and evolution of living
540   and fossil organisms, Annu. Rev. Earth Planet. Sci., 35, 541-576, 2007.
541   Rhein, M., Rintoul, S., Aoki, S., Campos, E., Chambers, D., Feely, R., Gulev, S., Johnson, G., Josey, S.,
542   Kostianoy, A., Mauritzen, C., Roemmich, D., and Wang, L. T. a. F.: Observations: Ocean. In: Climate

543   Change 2013: The Physical Science Basis. Contribution of Working Group I to the Fifth Assessment
544   Report of the Intergovernmental Panel on Climate Change Cambridge Univetsity Press, Cambridge,
545   United Kingdom and New York, NY, USA, , 1535 pp., 2013.
546   Ries, J. B.: Skeletal mineralogy in a high-CO_2 world, Journal of Experimental Marine Biology and
547   Ecology, 403, 54-64, 2011.
548   Ries, J. B., Cohen, A. L., and McCorkle, D. C.: Marine calcifiers exhibit mixed responses to CO_2-
549   induced ocean acidification, Geology, 37, 1131-1134, 2009.
550   Romeed, S., Fok, S., and Wilson, N.: A comparison of 2D and 3D finite element analysis of a restored
551   tooth, Journal of oral rehabilitation, 33, 209-215, 2006.
552   Starko, S., Claman, B. Z., and Martone, P. T.: Biomechanical consequences of branching in flexible
553   wave-swept macroalgae, New Phytologist, 206, 133-140, 2015.
554   Tanur, A., Gunari, N., Sullan, R., Kavanagh, C., and Walker, G.: Insight into the composition,
555   morphology, and formation of the calcareous shell of the serpulid hydroides dianthus, Journal of
556   Structural Biology, 169, S5-S20, 2010.
557   Wang, R. Z., Addadi, L., and Weiner, S.: Design strategies of sea urchin teeth: structure, composition
558   and micromechanical relations to function, Philosophical Transactions of the Royal Society of
559   London. Series B: Biological Sciences, 352, 469-480, 1997.
560   Weiner, S., Addadi, L., and Wagner, H. D.: Materials design in biology, Materials Science and
561   Engineering: C, 11, 1-8, 2000.
562   Zienkiewicz, O., Taylor, Z., and Zhu, J.: The finite element method: its basis and fundamentals.
563   Butterworth-Heinemann, Amsterdam, 2005.

564

565 Tables

566 Table 1 Mesh type, number of elements, average von Mises Stress, 95th percentile of (Mises)

567 Stress and Total Strain energy for the different models

Model	Mesh type	Number of Elements	Average von Mises Stress (Pa)	95 percentile of von Mises Stress (Pa)	Total Strain Energy (J)
422 µatm 2D model	Quad	16368	1.67E+11		8.91E08
589 µatm 2D model	Quad	1889	5.17E+11		1.27E10
3D	hexagonal	202304	1.72E+11		1.11E11
3D*	hexagonal	202304			4.70E11
3D (Corridor model)	tetrahedral	2125549	7.46E+10	2.21E+11	1.75E10
422 µatm compartmentalised (Compartment model)	tetrahedral	3442433	2.75E+10	5.36E+10	4.28E09
589 µatm compartmentalised (OA model)	tetrahedral	1707673	4.98E+10		8.81E09
Biologically realistic model (Biological model)	tetrahedral	2106858	2.74E+10	5.63E+10	5.21E9

568 *Strain energy corrected for calcite volume

569 Table 2 Percentage volumes of calcite and cavities in the biological model, the corridor and

570 the compartment model.

	Biological Model	3D Corridor model	3D Compartment model
volume of calcite (µm^3)	3.09E+05	1.94E+05	2.87E+05
volume of cavities (µm^3)	1.83E+05	2.60E+05	1.67E+05
percentage of calcite	63%	43%	63%
percentage of cavities	37%	57%	37%

571

572

573 Table 3 Average von Mises Stress, 95th percentile of (Mises) Stress and Total Strain energy for the
574 different load types exerted on the biological, compartment and corridor models. Total strain energy
575 for the biological model has been corrected for calcite volume (equation 2). The compartment
576 model under the shear loading type is highlighted to reiterate that the loading setup is different to
577 the biological model under a shear loading type.

Model	Loading Type	Average Stress (N μm^{-2})	95th Percentile of (Mises) Stress (N μm^{-2})	Total Strain Energy (J)
Biological				
	Compressive	2.34E-04	4.08E-04	3.34E+05
	Shear	2.83E-04	6.07E-04	6.11E+05
	Original (Shear + Compressive)	3.49E-04	7.21E-04	9.73E+05
Compartment				
	Compressive	2.42E-04	2.96E-04	2.34E+05
	Shear	4.27E-04	1.03E-03	1.63E+06
	Original (Shear + compressive)	4.10E-04	8.25E-04	9.63E+05

578

579 Table 4 Average von Mises Stress and Total Strain energy for the comparison of the different
580 material properties in the 2D and 3D corridor models

	Young's Modulus (Pa)	Average Von Mises Stress (Pa)	Total Strain energy (J)
2D Calcite	3.60E+10	1.67E+11	8.91E+08
M.edulis -Min	4.39E+10	1.67E+11	7.30E+08
M.californianus -Min	4.79E+10	1.67E+11	6.69E+08
M.edulis -Max	7.18E+10	1.67E+11	4.47E+08
M.californianus -Max	7.93E+10	1.67E+11	4.04E+08
	Young's Modulus (Pa)	Average Von Mises Stress (Pa)	Total Strain energy (J)
3D corridor Calcite	3.60E+10	7.46E+10	1.75E+10
M.edulis -Min	4.39E+10	7.46E+10	1.43E+10
M.californianus -Min	4.79E+10	7.46E+10	1.31E+09
M.edulis -Max	7.18E+10	7.46E+10	8.77E+09
M.californianus -Max	7.93E+10	7.46E+10	7.94E+08

581
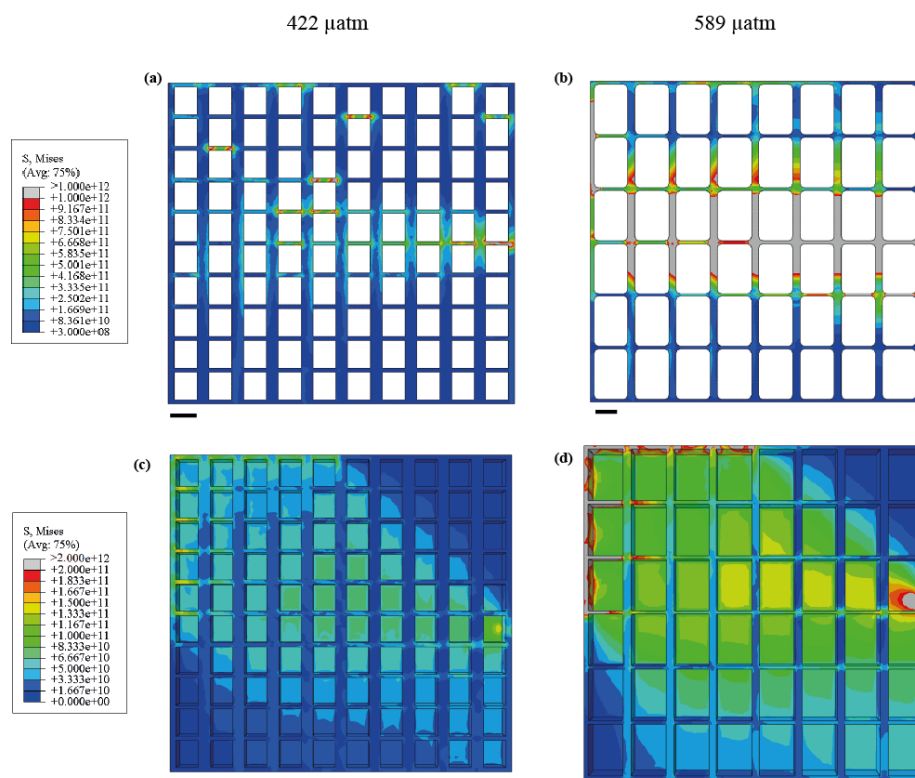
582   Figures
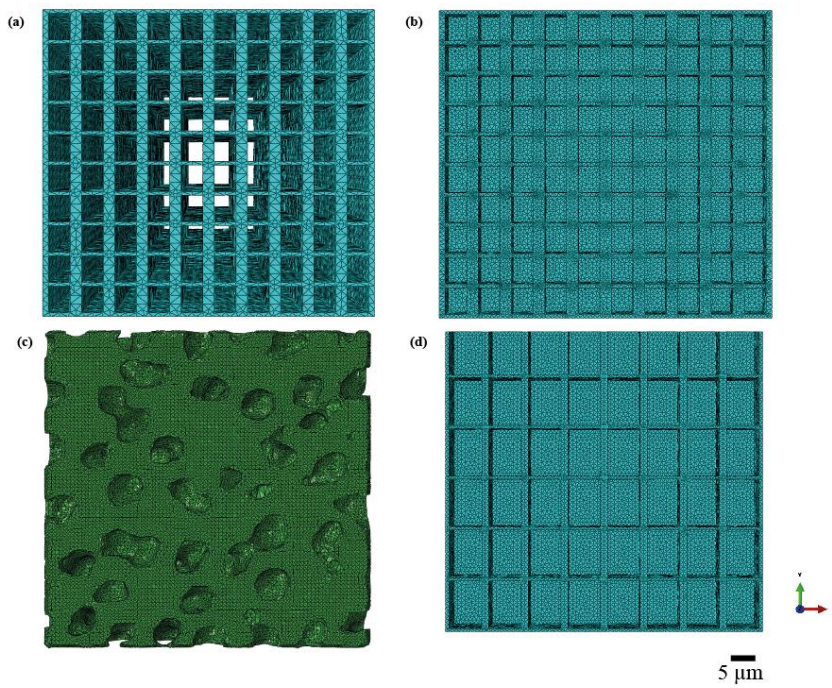
583   Figure 1
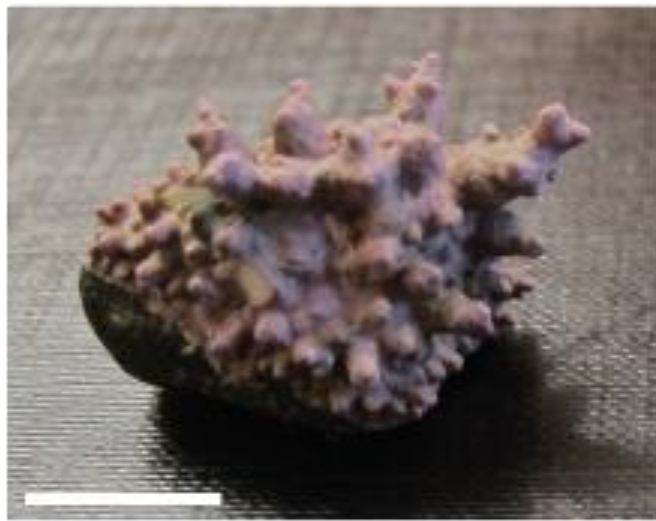
584
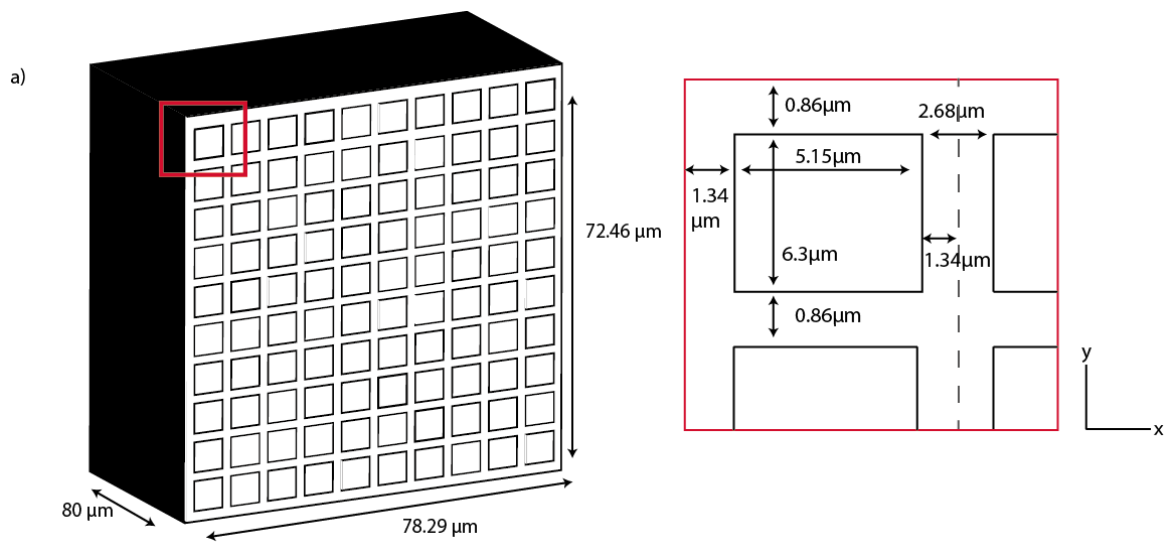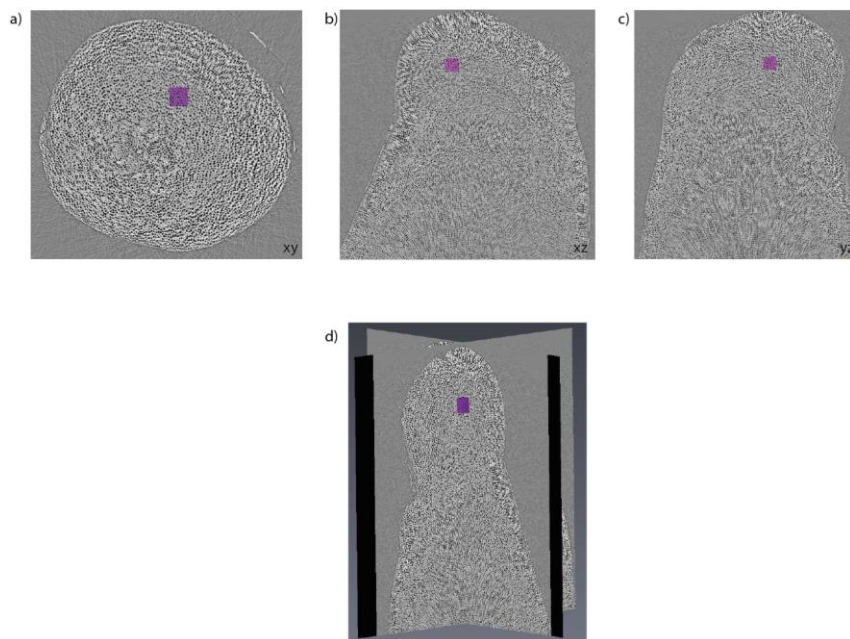
585   Figure 2

586

587

588   Figure 3

589

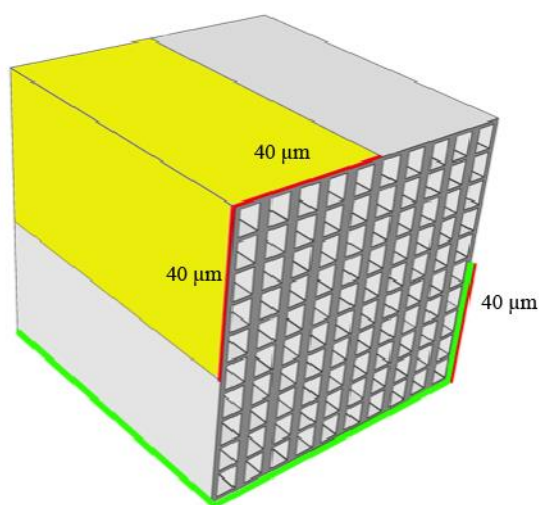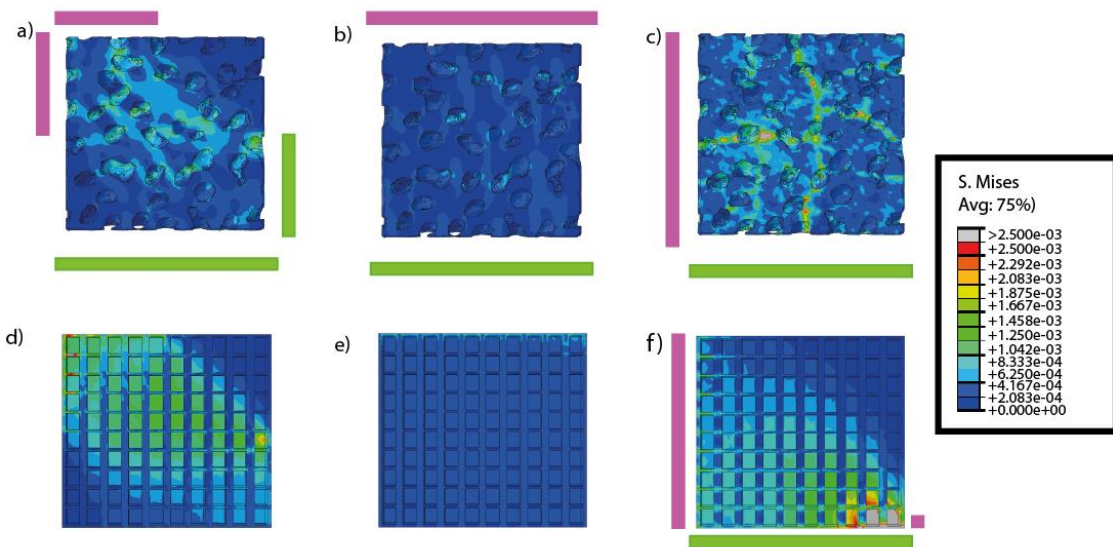590   Figure 4

591

592

593   Figure 5

594

595   Figure 6
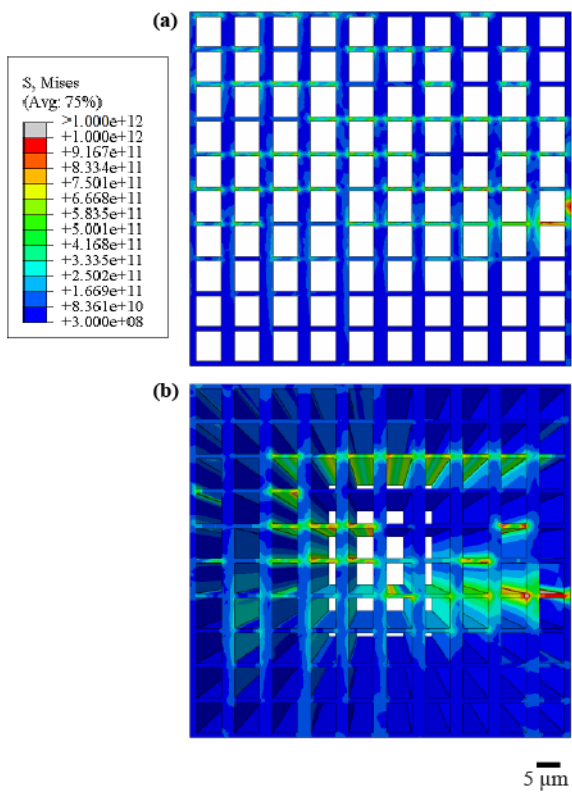

596

597

598   Figure 7

599

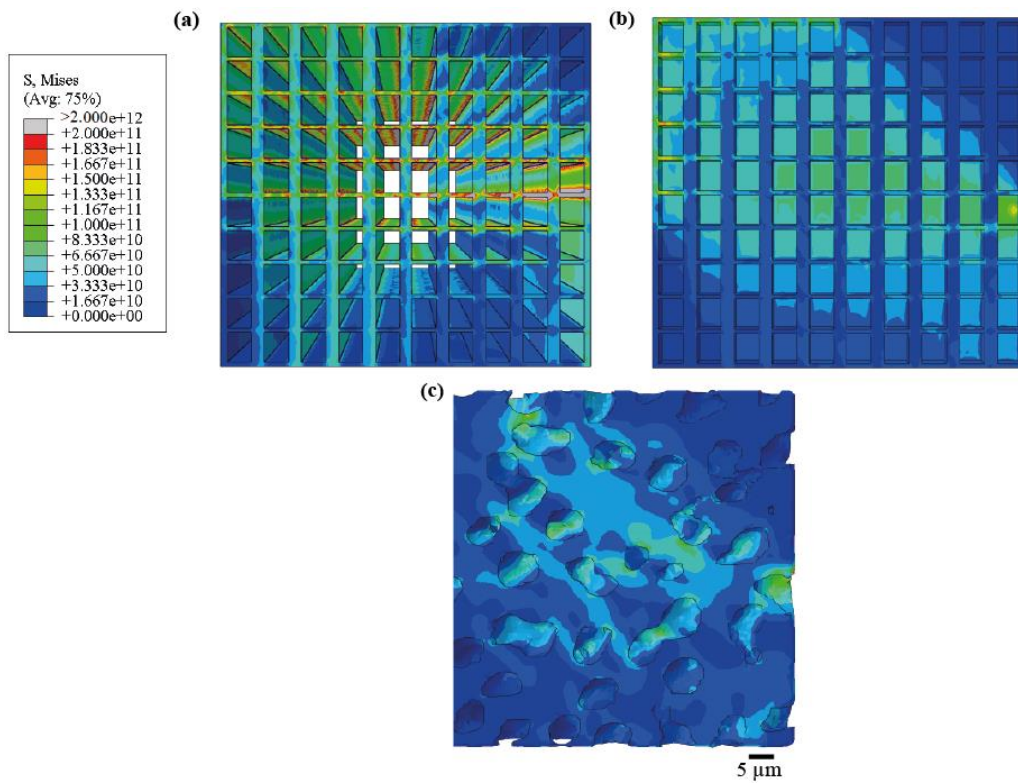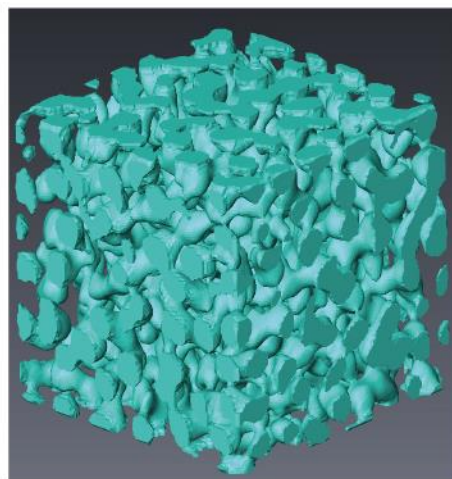600   Figure 8

601

602

603   Figure 9

604

605   Figure 10

606

607

608 Figure Legends

609 Figure 1: A *Lithothamnion glaciale* specimen in crustose form from Loch Creran, Oban,

610 Scotland; Scale = 1cm.

611 Figure 2: The effect of elevated CO_2 on the *Lithothamnion glaciale* structure. All models are

612 subjected to the same loads and boundary conditions and measurements taken from

613 Ragazzola et al. (2012). Von Mises Stresses are projected onto the 2D Finite element model

614 (a, b) and the 3D compartmentalised models (c, d). Warm colours indicate areas of high

615 stress, while cooler blue colours indicate areas of low stress. Units = PaFigure 3: The four

616 computer derived models; (a) The Corridor model, a simple 3D model; (b) The Compartment

617 model, a compartmentalised model; (c) The Biological model, the biologically realistic

618 model; (d) The OA model, the compartmentalised model under pCO_2 conditions simulating

619 the year 2050

620 Figure 4: Dimensions used in the 3D corridor model. Units =µm

621 Figure 5: Orthoslice projections in the different planes of a rhodolith thallus: a) xy direction;

622 b) xz direction; c) yz direction and d) in 3D format. The purple box highlights where the

623 80µm x 80µm cube was selected.

624 Figure 6: Loads and Boundary constraints. All models had the same loads and constraints

625 applied. Loads, representing wave erosion, were applied to the top left hand corner along a

626 strip 40µm wide at the external top left side of the model (yellow surface). Constraints were

627 applied to the bottom right corner (opposite corner to load) along a strip 40µm wide up the

628 right hand side of the model and over the whole of the bottom model (green lines).

629 Figure 7: The von Mises Stress patterns on the biological model (a, b & c) and the

630 compartment model (d, e & f) in different loading situations; the original (mixture of both

631   shear and compressive loads) (a & d); compressive load (b & e) and the shear load (c & f).

632   The different load situations (pink box) are shown on the biological model as well as the

633   constraints (green boxes). The shear load for the compartment model was set up slightly

634   differently and hence the loading setup is displayed on the model (f). Units = N μm^{-2}.

635   Figure 8: (a) 2D vs (b) 3D comparison of the *Lithothamnion glaciale* structure based on

636   Ragazzola et al. (2012) measurements. Units = Pa

637   Figure 9: Comparison of all 3D models. (a) The 3D corridor model (b) the compartment

638   model and (c) the biological model. Units = Pa.

639   Figure 10: The inside spheroidal cavities of the biological model